Ultrafast Science
A SCIENCE PARTNER JOURNAL

RESEARCH ARTICLE

Line Shape Relations in Ultrafast Transient Absorption from a Coherent Superposition

Chunyuan Bai[1,2], Chun Huang[1,2], Hongtao Hu[3], Mathew Britton[4], Marianna Lytova[5], Zhongyao Yue[1,2], Xiaojing Liu[1,2], Ruxin Li[1], David M. Villeneuve[6,7], and Peng Peng[1,2*]

[1]School of Physical Science and Technology, ShanghaiTech University, Shanghai 201210, China. [2]Center for Transformative Science, ShanghaiTech University, Shanghai 201210, China. [3]Photonics Institute, Technische Universität Wien, A-1040 Vienna, Austria. [4]Linac Coherent Light Source, SLAC National Accelerator Laboratory, Menlo Park, CA 94025, USA. [5]INRS-EMT, Varennes, Quebec J3X 1P7, Canada. [6]Joint Attosecond Science Laboratory, National Research Council and University of Ottawa, Ottawa, ON K1A 0R6, Canada. [7]Department of Physics, University of Ottawa, Ottawa, ON K1N 6N5, Canada.

*Address correspondence to: pengpeng@shanghaitech.edu.cn

Citation: Bai C, Huang C, Hu H, Britton M, Lytova M, Yue Z, Liu X, Li R, Villeneuve DM, Peng P. Line Shape Relations in Ultrafast Transient Absorption from a Coherent Superposition. *Ultrafast Sci.* 2026;6:Article 0165. https://doi.org/10.34133/ultrafastscience.0165

Submitted 28 November 2025
Revised 1 April 2026
Accepted 27 April 2026
Published 10 June 2026

Ultrafast laser pulses with broad bandwidth can simultaneously excite multiple quantum states, forming coherent superpositions. The phases of the associated optical transitions evolve in time, giving rise to spectral line profiles that range from symmetric Lorentzian to asymmetric Fano-like forms. Yet, the line shape relations between different transitions within such superpositions remain largely unexplored. Here, we use transient absorption spectroscopy to probe transitions from coherent superpositions. While each transition's line profile evolves over time, the relative line shape relations between different transitions remain fixed. We identify 4 fundamental types of line shape relations, each producing distinct spectral signatures. These relations naturally arise from second-order perturbation processes and can be actively tuned via the laser–matter interaction strength. Our findings establish a pathway for line shape-engineered control across atomic and molecular systems.

Introduction

The advent of femtosecond and attosecond laser sources has transformed transient absorption spectroscopy (TAS) into a powerful tool for probing ultrafast dynamics [1–33], including the electron motion [4,5], laser-controlled Fano resonances [6–8], and Raman time delays [12]. In a typical pump–probe scheme, a short pump pulse excites multiple quantum states simultaneously, creating a coherent superposition, which is then interrogated by a delayed probe pulse that induces dipole transitions and generates free induction decay (FID). The resulting absorption signal arises from interference between the probe field and the emitted FID. In general, an absorption signal is characterized by its strength, line shape, and resonance energy. Among these, the absorption line shape has received considerable attention in recent years [5–7]. Generally, spectral line shapes can be classified as symmetric Lorentzian or asymmetric Fano profiles. The Lorentzian line shape arises from transitions between discrete bound states below the ionization threshold, leading to a symmetric spectral response. In contrast, Fano line shapes emerge when a discrete state is coupled to a continuum of states, resulting in a characteristic asymmetric spectral profile. A new perspective was introduced in 2013 by Ott et al. [6], in which these spectral line shapes were interpreted in terms of the phase of the induced dipole response. Within this framework, Lorentzian and Fano profiles correspond to different dipole phases.

Previous TAS studies of line shapes have revealed phase control of 2-electron wave packets [5], ultrafast buildup of Fano resonances [7], and self-modulation effects in single-pulse excitation [16]. These investigations primarily focused on individual transitions. While they provide deep insight into single-state dynamics, they do not account for the fact that transitions within a coherent superposition are inherently connected. Quantum coherence links multiple states, establishing intrinsic relations among different transitions. These connections are crucial for understanding how interference emerges in multilevel systems and how the collective dynamics of a wave packet influence spectral signatures. Despite their importance, the relations between different transitions, particularly their relative phases, remain largely unexplored. Theoretically, the Hermitian nature of the density matrix predicts that phases of transitions coupled by the same coherence are additive inverses [23,26,29]; however, a comprehensive experimental verification is still lacking. Moreover, it remains unknown whether other types of phase relations exist or whether these relations can be actively controlled by tuning experimental parameters.

Here, we employ TAS to investigate line shape (dipole phase) relations between transitions in 2 distinct systems: rubidium (Rb) atoms and molecular hydrogen (H_2). A short femtosecond

pump pulse creates a 2-state superposition, which is then coupled to a third state by a delayed probe pulse, forming a coherent 3-level system. We demonstrate that the dynamic coherence phases modulate spectral line shapes of individual transitions, which evolve from symmetric Lorentzian to asymmetric Fano-like profiles depending on the pump–probe delay. Detailed line shape analysis reveals 4 fundamental dipole phase relations, each giving rise to distinct spectral signatures. Notably, for a fixed laser intensity and medium density, the phase relations between transitions remain constant across all time delays, even as the individual transition phases evolve. Different phase relations can be selectively accessed by adjusting the laser–matter interaction strength. These results uncover the intrinsic phase structure of coherent superpositions and provide a pathway for line shape-engineered control in diverse atomic and molecular systems.

Materials and Methods

Rb experiments

In the Rb experiment, the output of a commercial Ti:sapphire amplifier (1 kHz, 8 mJ, 780 nm, 25 fs) was used as both pump and probe. These 2 beams propagated noncollinearly and intersected inside an absorption cell containing Rb vapor, with a crossing angle of 3 mrad. The vapor cell is 50 mm in length and sealed with two 1-mm-thick BK7 glass windows at both ends. The temperature was varied between 70 and 120 °C using a custom-built heating and control system, and the Rb vapor densities ($\sim 10^{14}$ cm^{-3}) were estimated from the corresponding vapor pressures [14]. After interacting with the sample, the transmitted probe beam was collected using an integrating sphere and analyzed with a fiber-coupled spectrometer (Ocean Optics HR4000, resolution: 0.15 meV @ 1.5 eV). The intensities of the pump and probe beams were independently tuned to approximately 10^9 W / cm^2 using continuously variable neutral-density filters, remaining well below the laser filamentation threshold in the front window.

H_2 experiments

The H_2 experiments were performed at a high harmonic generation (HHG) beamline that was previously described in detail [15]. Approximately 1.6 mJ of near-infrared (NIR) laser pulse was sent into a differentially pumped hollow core fiber (250 μm inner diameter) filled with 0.7 bar of argon to create a 10-fs pulse centered around 800 nm. This pulse was focused into a pulsed gas jet of xenon (3 bar backing pressure, 250 μm nozzle) where HHG took place. A 500-μm-diameter pinhole and 2 silicon mirrors were employed to block the residual NIR driving field and transmit most of the extreme ultraviolet (XUV) radiation. An intensity of 2×10^{11} W / cm^2 was estimated for the residual NIR pulse at the sample target based on the Stark shift. Notably, all results reported in this study remain reproducible when the pinhole is replaced by a 350-nm-thick indium foil. A replica of the 10-fs NIR pulse was used as the pump pulse to perform impulsive alignment of the H_2 molecules. The maximum alignment degree is estimated to be 0.35 based on numerical simulations performed using the experimental parameters $I = 3 \times 10^{13}$ W / cm^2, $\tau = 10$ fs, and $T = 100$ K. The NIR pump pulse was combined with the XUV probe pulse with a holey mirror. The XUV and the NIR pulses propagated noncollinearly and intersected at the absorption gas jet (250 μm nozzle, gas density $\sim 10^{17}$ cm^{-3}, interaction length ~ 0.5 mm) with a crossing angle of 18 mrad. The transmitted XUV spectrum was dispersed in a flat-field XUV spectrometer and detected by a microchannel plate detector. The XUV spectrometer was set around 12 eV to achieve the high spectral resolution of 15 meV.

Line shape analysis

The measured absorption line shape is fitted with Eq. 1. The photon energy ω, pump–probe delay τ, and resonance energy ω are extracted directly from the measured data. The linewidth Γ is fixed based on the spectrometer resolution, which is 0.15 meV for Rb and 15 meV for H_2. By adjusting the dipole response phase $\phi(\tau)$, strength a, and offset b, we obtained the best-fit line shapes $\sigma(\omega, \tau)$ using a least-squares fitting procedure. A full comparison of the measured and fitted 2-dimensional spectra is available in Section S3.

Results

Schematic of pump–probe experiment

Figure 1A and B illustrates the pump–probe schemes implemented in 2 types of 3-level superpositions excited by femtosecond laser pulses: a V-type system in Rb and a Λ-type system in H_2. In the case of Rb, a NIR pump pulse prepares an electronic coherence, shown in the density matrix as $\rho_{1/2,3/2}$, between the $5p_{1/2}$ and $5p_{3/2}$ excited states [15,16]. A delayed NIR probe pulse then interrogates this coherence by simultaneously driving 2

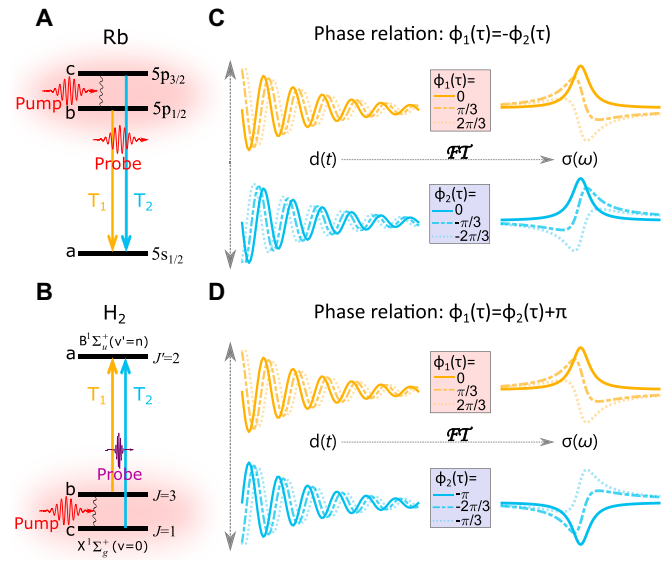

Fig. 1. Phase relations between transitions in 2 distinct systems. (A) V-type system in Rb. A NIR pump pulse prepares an electronic quantum coherence, $\rho_{1/2,3/2}$ between the $5p_{1/2}$ and $5p_{3/2}$ excited states. A delayed NIR probe pulse then interrogates this coherence by simultaneously driving 2 dipole-allowed transitions to the $5s_{1/2}$ ground state, labeled as T_1 ($5p_{1/2} \rightarrow 5s_{1/2}$) and T_2 ($5p_{3/2} \rightarrow 5s_{1/2}$). (B) Λ-type system of H_2. A NIR pump pulse creates a rotational coherence, $\rho_{1,3}$, between the rotational states $X^1\Sigma_g^+$ ($v = 0, J = 1$) and $X^1\Sigma_g^+$ ($v = 0, J = 3$). This rotational superposition is subsequently probed by a time-delayed broadband extreme ultraviolet (XUV) pulse, which simultaneously drives 2 dipole transitions to the excited state $B^1\Sigma_u^+$ ($v' = n, J' = 2$). The 2 transitions are labeled as T_1 ($J = 3 \rightarrow J' = 2$) and T_2 ($J = 1 \rightarrow J' = 2$). (C) FID $d(t)$ and corresponding absorption line shape $\sigma(\omega)$ of transition T_1 (yellow) and transition T_2 (blue) at different delay τ, the phase relation $\phi_1(\tau) = -\phi_2(\tau)$ holds. (D) Same as in (C), but with the phase relation $\phi_1(\tau) = \phi_2(\tau) + \pi$.

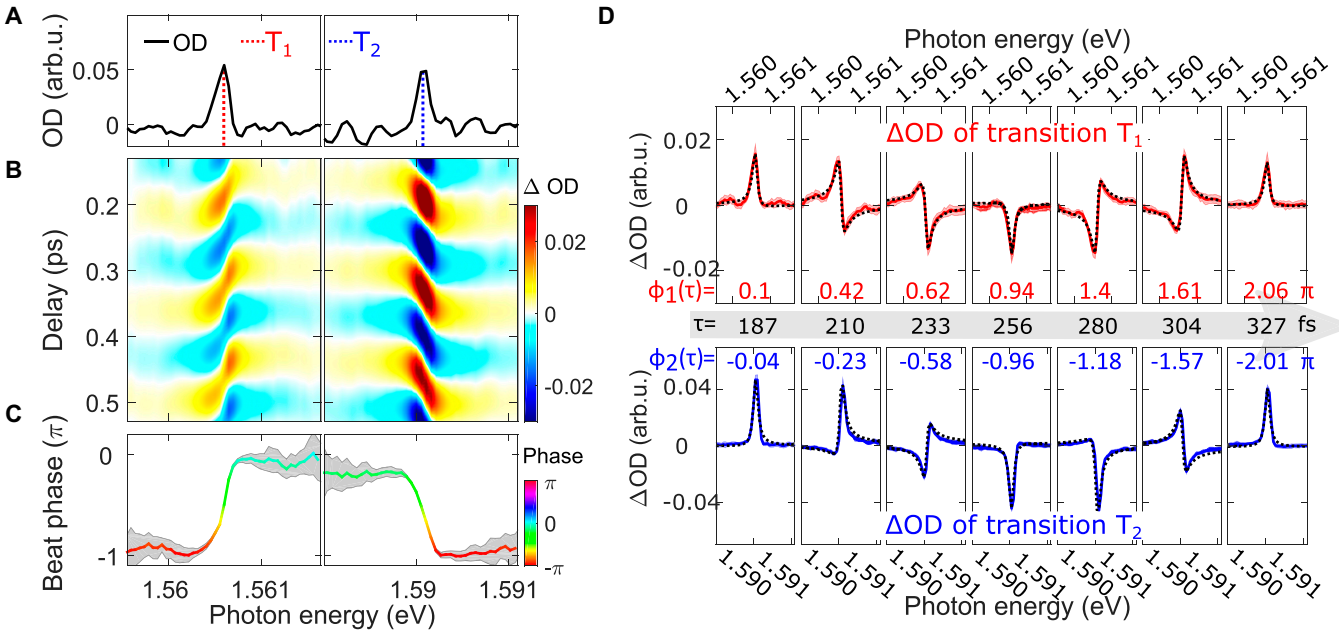

Fig. 2. Transient absorption in Rb. (A) Measured static absorption of Rb. The peaks of $T_1\,(5p_{1/2} \rightarrow 5s_{1/2})$ and $T_2\,(5p_{3/2} \rightarrow 5s_{1/2})$ transition are marked with dashed red and blue lines, respectively. (B) Experimental differential absorption spectra ΔOD. Significant quantum beats are observed at the T_1 and T_2 transitions. Notably, the modulation signals exhibit a phase difference between these transitions, resulting in a characteristic hat-shaped structure. (C) Phase of the quantum beat as a function of photon energy. The phase varies from $-\pi$ to 0 then back to $-\pi$. The shaded regions represent the standard deviation of over 15 independent measurements. (D) Lineouts of experimental ΔOD of transition T_1 (red) and transition T_2 (blue). The line shape changes between a symmetric Lorentzian profile and an asymmetric Fano profile. At each delay, the 2 transitions exhibit different line shapes. Line shape analysis allowed us to extract the dipole response phase $\phi_1(\tau)$ and $\phi_2(\tau)$, as indicated by the red and blue numbers. The black dotted curves show the calculated line shapes by using the extracted phase $\phi(\tau)$, which closely match the experimental results.

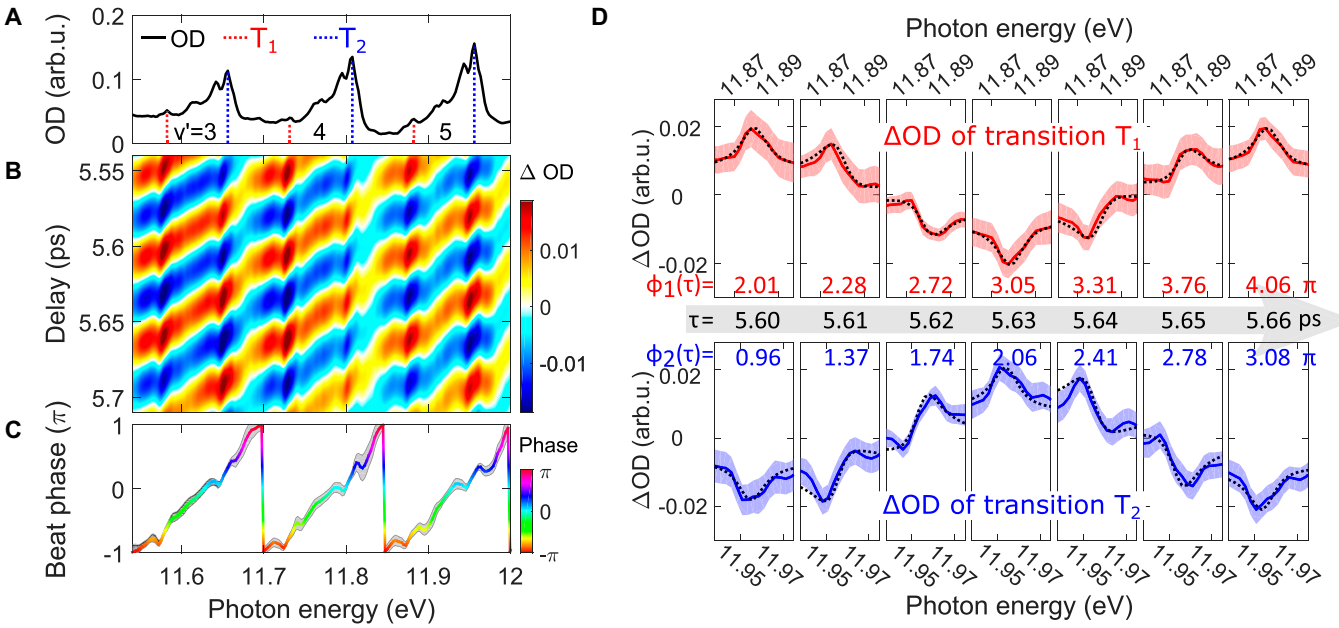

Fig. 3. Transient absorption in H_2. (A) Measured static absorption of isotropic H_2 molecules. Vibrational levels $v' = 3, 4, 5$ were selected as representative examples of the upper states to simplify the discussions, although similar results were observed for other upper states with different v'. The peaks of T_1 and T_2 transitions are marked with dashed red and blue lines, respectively. (B) Experimental differential absorption spectra ΔOD. The evolving line shapes produce a twill-like structure, distinct from the hat-shaped pattern observed in Rb. (C) Beat phase as a function of photon energy. For each v', the phase changes monotonically from $-\pi$ to π. The shaded regions represent the standard deviation of over 15 independent measurements. (D) Lineouts of experimental ΔOD of transition T_1 (red) and transition T_2 (blue). Line shape analysis allowed us to extract the dipole response phase $\phi(\tau)$, as indicated by the red and blue numbers. The black dotted curves show the calculated line shapes by using the extracted phase $\phi(\tau)$.

dipole-allowed transitions to the $5s_{1/2}$ ground state, labeled as T_1 $\left(5p_{1/2} \rightarrow 5s_{1/2}\right)$ and T_2 $\left(5p_{3/2} \rightarrow 5s_{1/2}\right)$. For H_2, the NIR pump pulse creates a rotational coherence, $\rho_{1,3}$, between the states $X^1\Sigma_g^+$ $(v=0, J=1)$ and $X^1\Sigma_g^+$ $(v=0, J=3)$ [18]. This rotational superposition is subsequently probed by a time-delayed broadband XUV pulse, which simultaneously drives 2 dipole transitions to the electronically excited state $B^1\Sigma_u^+$ $\left(v'=n, J'=2\right)$. These 2 transitions are labeled as T_1 $\left(J=3 \rightarrow J'=2\right)$ and T_2 $\left(J=1 \rightarrow J'=2\right)$. Figure 1C and D shows the corresponding FID fields, $d(t)$, generated by transition T_1 and transition T_2, depicted as yellow and blue curves, respectively. Their associated phases are denoted $\phi_1(\tau)$ and $\phi_2(\tau)$, where τ is the delay between pump and probe pulses. The absorption cross-section is defined as $\sigma(\omega) \propto \mathrm{Im}[d(\omega)]$, where $d(\omega)$ is the Fourier transforms of the FID field. As the coherence ($\rho_{1/2,3/2}$ for Rb or $\rho_{1,3}$ for H_2) evolves in time, the phases $\phi_1(\tau)$ and $\phi_2(\tau)$ are modulated accordingly, leading to characteristic changes in the absorption line shapes. Crucially, the phase relation between $\phi_1(\tau)$ and $\phi_2(\tau)$, i.e., $\phi_1(\tau) = -\phi_2(\tau)$ in Fig. 1C and $\phi_1(\tau) = \phi_2(\tau) + \pi$ in Fig. 1D, can be directly extracted from a line shape analysis.

Transient absorption in Rb

In the experiment of Rb, 25-fs NIR pulses centered at 780 nm were used as both pump and probe. The 2 beams propagated noncollinearly and intersected inside a 50-mm-long absorption cell containing Rb vapor, with a crossing angle of 3 mrad. This configuration was chosen to ensure sufficient spatial overlap of the 2 beams throughout the cell while allowing clear spatial separation at the collection optics located 2 m downstream (Section S1). After interacting with the sample, the transmitted probe beam was collected by an integrating sphere and analyzed using a fiber-coupled spectrometer (Materials and Methods provides more details). The intensities of the pump and probe beams were independently adjusted to approximately 10^9 W / cm^2 using continuously variable neutral-density filters. The Rb vapor density, estimated to be on the order of 10^{14} cm^{-3} [16], was controlled via a homemade heating system. The time delay between the pump and probe pulses was precisely varied using a motorized translation stage, with positive delay defined such that the pump pulse precedes the probe.

Figure 2A shows the static absorption spectrum of Rb measured without the NIR pump, featuring 2 absorption lines, T_1 and T_2, centered at 1.56 and 1.59 eV, respectively. Figure 2B shows the measured transient absorption spectra, defined as $\Delta\mathrm{OD}(\omega,\tau) = -\log\left[I_{on}(\omega,\tau)/I_{off}(\omega,\tau)\right]$. Here, $I_{on}(\omega,\tau)$ and $I_{off}(\omega,\tau)$ are the probe spectra after transmission through the sample with and without the pump field, respectively. To enhance the visibility of the quantum beat signal, a Fourier filter between 5 and 9 THz was applied (Section S2). Both transitions exhibit pronounced oscillations with a periodicity of 140 fs (beating frequency of 7 THz), corresponding to the 29.4-meV energy splitting of the $5p_{1/2}$ and $5p_{3/2}$ states. The overall ΔOD spectrum exhibits a distinctive hat-shaped structure, reflecting the delay-dependent modulation of the line shapes. Figure 2C shows the phase of the quantum beat as a function of photon energy. The shaded regions represent the standard deviation of over 15 independent measurements. The beat phase evolves from $-\pi$ to 0 and back to $-\pi$, consistent with previous theoretical predictions [23,26,29]. Figure 2D shows spectral lineouts of ΔOD for transition T_1(red) and T_2(blue). Notably, the line shape of each transition varies between a symmetric Lorentzian and an asymmetric Fano profile, and the 2 transitions exhibit distinct line shapes at each delay. The FID phase, $\phi(\tau)$, was extracted by fitting the measured absorption line shape to the function [22,24]

$$\sigma(\omega,\tau) = a\left\{\cos[\phi(\tau)]\frac{\frac{\Gamma}{2}}{(\omega_0-\omega)^2+\frac{\Gamma^2}{4}} + \sin[\phi(\tau)]\frac{(\omega_0-\omega)}{(\omega_0-\omega)^2+\frac{\Gamma^2}{4}}\right\} + b, \quad (1)$$

where the main component inside the curly brackets determines the spectral line shape, ω is the photon energy, τ is the pump–probe delay, ω_0 is the resonance energy, Γ is the decay rate of the excited state, and a and b represent the signal strength and the background offset (Materials and Methods provides more details). This expression consists of absorptive (first term) and dispersive (second term) components, whose relative weights are governed by $\phi(\tau)$. By varying $\phi(\tau)$, we determined the line shapes that best reproduced the experimental data using a least-squares fitting procedure. The fitted profiles are shown as black dashed curves in Fig. 2D, with the extracted values of $\phi_1(\tau)$ and $\phi_2(\tau)$ indicated in red and blue, respectively. A full comparison of the measured and fitted 2-dimensional spectra is available in Section S3. This procedure was repeated for all time delays, and the resulting FID phases are plotted in Fig. 4A (the full 2-dimensional comparison was shown in Section S3). The sum $\phi_1(\tau) + \phi_2(\tau)$ remains close to zero at all delays (black dots), indicating that the 2 phases are additive inverses of each other, i.e., $\phi_1(\tau) = -\phi_2(\tau)$. Since the phase appears in the exponent as $e^{i\phi}$, opposite phases correspond to

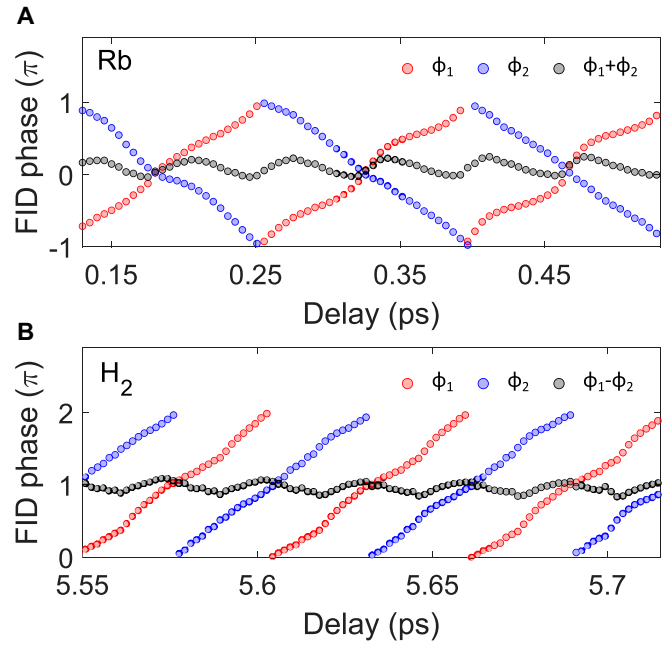

Fig. 4. FID phases extracted through line shape analysis. (A) FID phases of transition T_1 [$\phi_1(\tau)$, red] and T_2 [$\phi_2(\tau)$, blue] in Rb, the sum [$\phi_1(\tau) + \phi_2(\tau)$, black] remains close to zero across all delays. (B) FID phases of transition T_1 [$\phi_1(\tau)$, red] and T_2 [$\phi_2(\tau)$, blue] in H_2, the unwrapped phase difference [$\phi_1(\tau) - \phi_2(\tau)$, black] remains close to π across all delays.

complex conjugate (*c.c.*) values. We therefore refer to this as the *c.c.* relation.

Transient absorption in H_2

For the experiment with H_2, a 10-fs pump pulse was used to couple 2 rotational states $X^1\Sigma_g^+$ ($v=0, J=1,3$) via a Raman process, as the large rotational energy spacing of H_2 requires a broadband (i.e., short) pulse. A replica of the NIR pulse was then used to generate high harmonics in xenon, producing a broadband XUV pulse with a quasi-continuous spectrum in the detection energy range (11.4 to 13.5 eV), which was employed as the probe (Materials and Methods provides more details). This XUV probe drives dipole transitions from the prepared ground electronic state rotational coherence to the first electronically excited state, $B^1\ \Sigma_u^+\left(v'=m, J'=2\right)$. Due to the absence of strict vibrational selection rules in diatomic molecules and the broad bandwidth of the XUV pulse, the vibrational quantum number v' spans a wide range (from 0 to high values), while the rotational quantum number J' is restricted by the selection rules $J'-J=\pm 1$. For each v', an effective Λ-type 3-level system is formed. The resulting dipole responses give rise to 2 distinct absorption features, which were measured using a homebuilt XUV spectrometer with an energy resolution of 15 meV at 12 eV.

Figure 3A shows the static absorption spectrum of isotropic H_2 measured without the NIR pump. For clarity, we focus on 3 representative upper vibrational states, $v'=3,4,5$, although similar behavior was observed for other values v'. The transition T_1 and T_2 are marked by red and blue lines, respectively. Additional rotational transitions exist and partially overlapped with T_1 and T_2; however, they are one-channel transitions (involving only a single lower and upper state) and are delay-independent. They are effectively removed by constructing differential absorption spectra, ΔOD. Figure 3B shows the delay-dependent ΔOD spectrum, where a Fourier filter between 14 and 20 THz was applied to emphasize the quantum beat signal (Section S2). The long delay of approximately 5.7 ps ensures that the NIR pulse arrives marked earlier than the XUV pulse, thereby preventing contributions from multiphoton processes. The entire spectrum oscillates with a period of 60 fs (beating frequency of 17 THz), corresponding to the 69-meV energy difference between $X^1\Sigma_g^+$ ($v=0, J=1$) and $X^1\Sigma_g^+$ ($v=0, J=3$) states. The evolving line shapes produce a twill-like structure, distinct from the hat-shaped pattern observed in Rb. Figure 3C presents the beat phase as a function of photon energy. For each v', the phase varies monotonically from $-\pi$ to π. Figure 3D shows the spectral lineouts of the ΔOD spectrum for $v'=5$, with shaded regions representing the standard deviation across 15 independent measurements. Similarly, we extracted the FID phases $\phi_1(\tau)$ and $\phi_2(\tau)$ for transitions T_1 and T_2 by analyzing the corresponding line shape. The fitted profiles are shown as black dashed curves in Fig. 3D, with the extracted phase values indicated in red and blue, respectively. Figure 4B shows the retrieved FID phases over 3 cycles (the full 2-dimensional comparison is shown in Section S3). The unwrapped phase difference $\phi_1(\tau)-\phi_2(\tau)$ remains close to π at all delays (black dots), i.e., $\phi_1(\tau)=\phi_2(\tau)+\pi$, which we refer to as the π-relation.

Discussion

The phase behavior observed in our experiments differs from conventional phase-control schemes employing continuous-wave (cw) narrowband lasers. In the cw case, the amplitudes and phases of 2 excitation fields are adjusted to control the relative phase of pathways leading to the same final state. The excitation probability is then governed by the summed amplitudes, giving rise to phenomena such as electromagnetically induced transparency and coherent population trapping [34,35]. By contrast, a broadband femtosecond pump pulse in our experiments prepares a superposition that is subsequently interrogated by a delayed probe. The pump–probe delays (~500 fs for Rb and ~5.7 ps for H_2) are much longer than the pulse durations (~10 fs), so the pulses are well separated and the dynamics are dominated by the evolving quantum coherence. For each transition, the phase evolves with delay, producing delay-dependent absorption line shapes. Remarkably, even as the system dynamically evolves, the phase relations between different transitions coupled by a shared coherence remain fixed.

To elucidate the distinct phase relations observed in Rb and H_2, we applied the time-dependent perturbation theory to analyze the FID signal of a generic 3-level systems, with states labeled "a", "b", and "c". A pump pulse creates a superposition $A_b e^{i\phi_b(\tau)}|\psi_b\rangle + A_c e^{i\phi_c(\tau)}|\psi_c\rangle$ between "b" and "c", where A, ϕ, and $|\psi\rangle$ denote the amplitude, phase, and eigen-wavefunction, respectively. A subsequent probe pulse couples this superposition to state "a", resulting in the total wavefunction $|\psi(t,\tau)\rangle = C_a(t,\tau)|\psi_a\rangle + C_b(t,\tau)|\psi_b\rangle + C_c(t,\tau)|\psi_c\rangle$, with C representing complex expansion coefficients computed via the second-order perturbation theory (see Section S4 for detailed model of Rb and H_2). The resulting delay-dependent FID signals, $d_{Dyn,ba}(t,\tau)$ and $d_{Dyn,ca}(t,\tau)$, take the forms:

$$d_{Dyn,ba}(t,\tau)=2\times\mathrm{Re}\left\{ i\mu_{ba}A_cA_b\Omega_{ca}\left(\begin{array}{l}\left(1-|\Omega_{ba}|^2\right)e^{i[\phi_c(\tau)-\phi_b(\tau)]}\\ +|\Omega_{ba}|^2 e^{i[\phi_b(\tau)-\phi_c(\tau)+\pi]}\end{array}\right)e^{i(E_b-E_a)t-\Gamma_{ba}t}\right\}, \tag{2}$$

$$d_{Dyn,ca}(t,\tau)=2\times\mathrm{Re}\left\{ i\mu_{ca}A_cA_b\Omega_{ba}\left(\begin{array}{l}\left(1-|\Omega_{ca}|^2\right)e^{i[\phi_b(\tau)-\phi_c(\tau)]}\\ +|\Omega_{ca}|^2 e^{i[\phi_c(\tau)-\phi_b(\tau)-\pi]}\end{array}\right)e^{i(E_c-E_a)t-\Gamma_{ca}t}\right\}, \tag{3}$$

where μ is the transition dipole moment, Γ is the decoherence rate, $\Omega=\mu\int_{-\infty}^{\infty}f(t)dt$, and $f(t)$ is the envelope of probe pulse. Each FID signal comprises 2 phase-dependent terms, whose relative amplitudes are controlled by the interaction strength $|\Omega|^2$. When both $|\Omega_{ba}|^2$ and $|\Omega_{ca}|^2$ are less than 0.5, the first terms dominate in Eqs. 2 and 3, and the phases $\phi_1=\phi_c(\tau)-\phi_b(\tau)$ and $\phi_2=\phi_b(\tau)-\phi_c(\tau)$ are additive inverses of each other, consistent with the steady *c.c.* relation observed in Rb, where both transitions T_1 and T_2 exhibit weak absorption (~0.05, shown in Fig. 2A). In contrast, when $|\Omega_{ba}|^2$ is less but $|\Omega_{ca}|^2$ is larger than 0.5, the first term dominates $d_{Dyn,ba}(t,\tau)$, while the second dominates $d_{Dyn,ca}(t,\tau)$. The resulting phase terms $\phi_c(\tau)-\phi_b(\tau)$ and $\phi_c(\tau)-\phi_b(\tau)-\pi$ differ by π, yielding the steady π-relation. This is the case for H_2, where the absorption strength of T_2 (~0.2) significantly exceeds that of T_1 (~0.04), as shown in Fig. 3A. More precisely, when $|\Omega|^2$ in Eqs. 2 and 3 is neither 0 nor 1, 2 phase-dependent terms contribute simultaneously to the measured transient absorption signals, resulting in a mixed phase relation (Section S5). Consequently, the sum $\phi_1(\tau)+\phi_2(\tau)$ and difference $\phi_1(\tau)-\phi_2(\tau)$ of the extracted line shape phases exhibit weak oscillations around 0 and π, respectively, as shown by the black dots in Fig. 4.

The distinct behaviors observed in Rb and H_2 reveal that the underlying phase relation is not solely determined by the level

structure but instead governed by the interaction strength. In addition to the 2 relations previously discussed, Eqs. 2 and 3 predict 2 additional phase relations: (a) the anti-*c.c.* relation, given by $\phi_1 = \phi_b(\tau) - \phi_c(\tau) + \pi$ with $\phi_2 = \phi_c(\tau) - \phi_b(\tau) - \pi$, and (b) the anti-$\pi$ relation, where $\phi_1 = \phi_b(\tau) - \phi_c(\tau) + \pi$ with $\phi_2 = \phi_b(\tau) - \phi_c(\tau)$. Absorption spectra calculated for 4 relations were shown in Fig. 5A to D. The *c.c.* and π-relations produce hat-shaped and twill-shaped features, respectively, in close agreement with experimental observations (Figs. 2B and 3B). In contrast, the anti-*c.c.* and anti-π relations yield inverted-hat and inverted-twill structures.

It should be noted that our 3-level model is based on a single-atom description. However, in the actual experiment, an ensemble of systems with collective coupling is generally unavoidable. A rigorous treatment would require incorporating macroscopic propagation effects into the perturbative framework, which would substantially increase the complexity and is therefore beyond the scope of the present work. From a qualitative perspective, during light–matter interaction, the laser field modifies the properties of the medium, while the medium, in turn, reshapes the propagating light field. In particular, at higher densities, resonant interactions can significantly alter the temporal and spatial profiles of the pulse. Previous studies have shown that resonant propagation redistributes the spectral components of the laser field [14,16], enhancing some wavelengths while suppressing others. This process effectively acts as spectral shaping, thereby modifying the effective laser intensity at specific wavelengths and influencing the Rabi frequency experienced by the atoms. Therefore, in practical experiments, the interaction strength depends on both the laser intensity and the medium density. By tuning these parameters, the phase relation can be actively controlled. To explore this possibility, we use Rb as a platform to investigate phase control under varying experimental conditions. Since the cell is sealed with two 1-mm-thick BK7 glass windows, the laser intensity cannot be increased too high to avoid nonlinear effects in the windows. Consequently, we employ a combined strategy of tuning both the laser intensity and the medium density.

Figure 5E to H shows the measured transient absorption spectra of Rb under different pump intensities, probe intensities, and heating temperatures. All 2-dimensional spectra are normalized to their maximum intensity to facilitate comparison. A hat-shaped feature in Fig. 5A is observed at $I_{pump} = 1.2 \times 10^{10}$ W / cm^2, $I_{probe} = 5.7 \times 10^9$ W / cm^2, and $T = 70$ °C, consistent with the *c.c.* relation (Fig. 5E). Increasing the temperature from 70 °C to 120 °C raises the Rb vapor density and enhances absorption, producing a twill-like ΔOD spectrum associated with the π-relation (Fig. 5F). Lowering the pump intensity to 3×10^9 W / cm^2 transforms the spectral pattern into an inverted-hat structure, characteristic of the anti-*c.c.* relation (Fig. 5G). Conversely, reducing the probe intensity to 1.9×10^9 W / cm^2 yields an inverted-twill structure corresponding to the anti-π relation (Fig. 5H). While the overall spectral structure aligns well with theoretical calculations, deviations near resonance arise from a mixed-phase effect. By accounting for the simultaneous contributions of 2 phase-dependent terms, we extracted the interaction strengths $|\Omega|^2$ for each case (Section S5). The values of $|\Omega|^2$, along with the corresponding experimental conditions associated with the results presented in Fig. 5, are summarized in Table 1. Owing to the experimental challenges associated with the generation and control of attosecond XUV pulses, phase relation control was realized only in Rb in the present study. For H_2, we numerically solved the Liouville–von Neumann equation for a simplified 3-level system, which reproduced comparable spectral patterns under varying interaction strengths (Section S6). Altogether, these results demonstrate that the phase relation, and consequently the resulting spectral shape, can be deterministically controlled by tuning the laser–matter interaction strength.

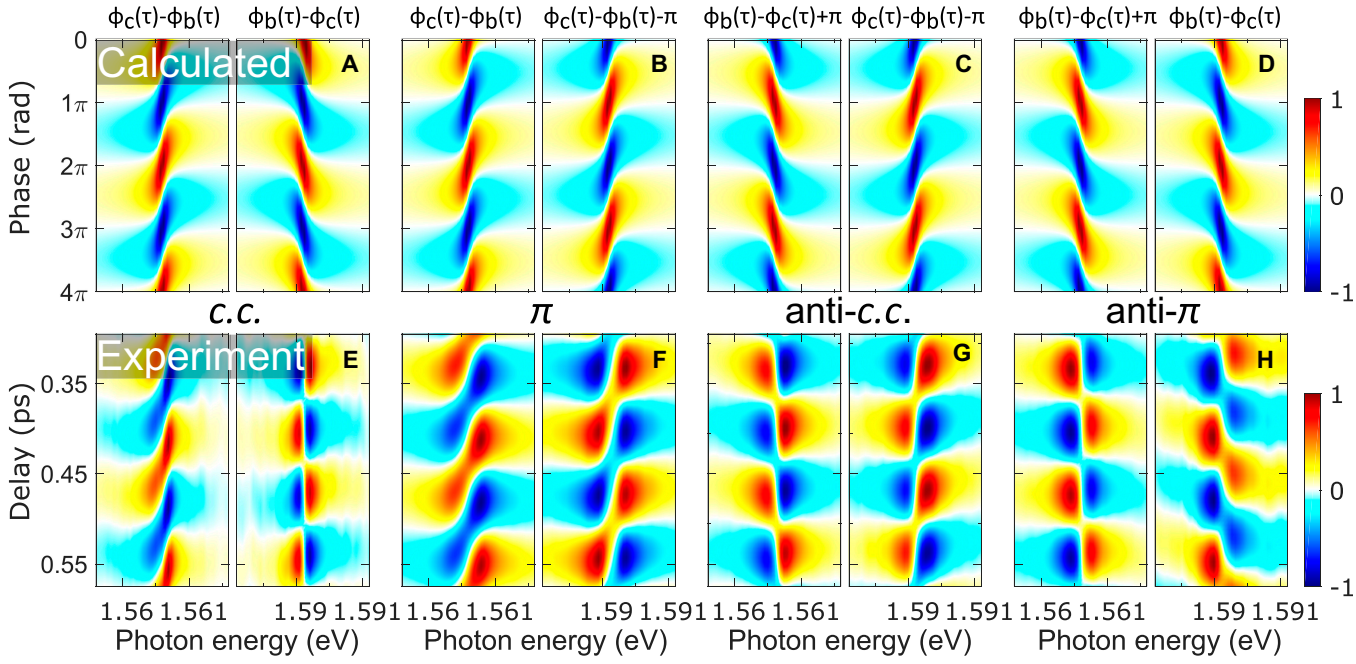

Fig. 5. Phase relation control in Rb. (A to D) Calculated absorption spectra for *c.c.*, π, anti-*c.c.*, and anti-π phase relations. Four distinct structures were observed: the hat, ladder, inverted-hat, and inverted-ladder features, respectively. (E to H) Experimental ΔOD in Rb under varying laser intensities and vapor densities, demonstrating the phase relation control.

Table 1. Summary of 4 phase relations and associated experimental conditions. The experimental results are shown in Fig. 5E to H. Errors shown are the range of each parameter such that the residual least-squares error between the model and the experiment increases by 10%.

	Experimental conditions			$\lvert\Omega\rvert^2$	
Relations	I_{pump} (W/cm^2)	I_{probe} (W/cm^2)	T (°C)	$\lvert\Omega_{T_1}\rvert^2$	$\lvert\Omega_{T_2}\rvert^2$
c.c. relation	1.2×10^{10}	5.7×10^{9}	70	$0.14^{+0.08}_{-0.11}$	$0.40^{+0.06}_{-0.07}$
π relation	1.2×10^{10}	5.7×10^{9}	120	$0.25^{+0.05}_{-0.05}$	$0.60^{+0.04}_{-0.04}$
Anti-*c.c.* relation	3.0×10^{9}	5.7×10^{9}	120	$0.60^{+0.05}_{-0.05}$	$0.59^{+0.07}_{-0.05}$
Anti-π relation	1.2×10^{10}	1.9×10^{9}	120	$0.66^{+0.06}_{-0.05}$	$0.32^{+0.09}_{-0.11}$

Conclusion

In conclusion, we have identified 4 fundamental line shape phase relations between transitions within a short-pulse-driven superposition: *c.c.*, π, anti-*c.c.*, and anti-π. These relations stem from the second-order perturbation processes and manifest as 4 distinct spectral features in TAS: hat-shaped, twill-shaped, inverted-hat-shaped, and inverted-twill-shaped structures. Although the entire system is dynamically evolving, the phase relations between different transitions coupled by a shared coherence remain stable across all pump–probe delays and can be actively controlled by varying the laser–matter interaction strength.

Our findings establish a benchmark for measuring and manipulating phase relations in quantum systems, offering new avenues for coherent control in ultrafast spectroscopy. Given the ubiquity of coherence in atomic, molecular, and condensed matter systems, this framework provides a universal strategy for tailoring quantum dynamics across diverse platforms, from cold atoms to ultrafast laser-driven plasmas. The ability to selectively engineer phase-dependent interactions deepens our understanding of phase-sensitive light–matter dynamics, which is crucial for a range of applications. For instance, in the N_2^+ air laser [36–38], characteristic emissions at 391 and 428 nm are observed, involving 3 electronic states, while the underlying gain mechanism remains only partially understood. High-resolution spectroscopic measurements further reveal that each emission line consists of multiple rotational transitions, whose intensities and line shapes can be controlled by varying the pump–probe delay and the carrier-envelope phase of the driving laser [39–41]. However, due to the large number of rotational levels involved in N_2^+, the resulting experimental observations are highly complex. One possible approach to simplify the system is to reduce the rotational-state distribution, for example, by cooling the molecular ensemble, thereby confining the Boltzmann population to a limited number of low-lying rotational states. In this context, the line shape analysis developed in our work may provide a useful framework for elucidating the generation mechanisms and enabling control of N_2^+ emissions. Looking ahead, extending these techniques to water-window high-harmonic sources or short-pulse x-ray free-electron lasers could enable coherent excitation of core-level electrons [24,42], opening the door to phase control in the x-ray regime.

Acknowledgments

We acknowledge the support of the Joint Centre for Extreme Photonics.

Funding: This work is supported by the National Key Research and Development Program of China (2024YFE0205700), the National Natural Science Foundation of China (12274297, 92250303, 12450405, and U23A6002), the Shanghai Rising-Star Program (22QA1406200), the Shanghai Science and Technology Program (21511105000), the start-up grant of ShanghaiTech University, the Double First-Class Initiative Fund of ShanghaiTech University, the Open Research Fund of State Key Laboratory of Quantum Functional Materials, and the NSERC Discovery Grant program (RGPIN-327147-2012) and by the U.S. Army Research Office through Award W911NF-14-1-0383. Part of this research used Beamline 03U of the Shanghai Synchrotron Radiation Facility, which is supported by the ME2 project under contract no. 11227902 from the National Natural Science Foundation of China.

Author contributions: P.P. and D.M.V. conceived and planned the experiment. C.B., Z.Y., C.H., and H.H. conducted the measurements. C.B., D.M.V., M.B., M.L., and P.P. analyzed and interpreted the data. X.L., R.L., D.M.V., and P.P. supervised the project. C.B. and P.P. wrote the manuscript, with input from all the authors.

Competing interests: The authors declare that they have no competing interests.

Data Availability

The data that support the findings of this study are available from the corresponding author upon reasonable request. The code used in this study is available from the corresponding author upon reasonable request.

Supplementary Materials

Sections S1 to S6
Figs. S1 to S8

References

1. Kling MF, Siedschlag C, Verhoef AJ, Khan JI, Schultze M, Uphues T, Ni Y, Uiberacker M, Drescher M, Krausz F, et al.

Control of electron localization in molecular dissociation. *Science*. 2006;312(5771):246–248.
2. Martín F, Fernández J, Havermeier T, Foucar L, Weber T, Kreidi K, Schöffler M, Schmidt L, Jahnke T, Jagutzki O, et al. Single photon-induced symmetry breaking of H_2 dissociation. *Science*. 2007;315(5812):629–633.
3. Zhang P, Liang H, Han M, Trester J, Ji J, Rost JM, Wörner HJ. Resolving the phase of Fano resonance wave packets with photoelectron frequency-resolved optical gating. *Nat Photonics*. 2025;19(8):847–853.
4. Goulielmakis E, Loh Z-H, Wirth A, Santra R, Rohringer N, Yakovlev VS, Zherebtsov S, Pfeifer T, Azzeer AM, Kling MF, et al. Real-time observation of valence electron motion. *Nature*. 2010;466(7307):739–743.
5. Ott C, Kaldun A, Argenti L, Raith P, Meyer K, Laux M, Zhang Y, Blättermann A, Hagstotz S, Ding T, et al. Reconstruction and control of a time-dependent two-electron wave packet. *Nature*. 2014;516(7531):374–378.
6. Ott C, Kaldun A, Raithet P, Meyer K, Laux M, Evers J, Keitel CH, Greene CH, Pfeifer T. Lorentz meets Fano in spectral line shapes: A universal phase and its laser control. *Science*. 2013;340(6133):716–720.
7. Kaldun A, Blättermann A, Stooß V, Donsa S, Wei H, Pazourek R, Nagele S, Ott C, Lin CD, Burgdörfer J, et al. Observing the ultrafast buildup of a Fano resonance in the time domain. *Science*. 2016;354(6313):738–741.
8. Kaldun A, Ott C, Blättermann A, Laux M, Meyer K, Ding T, Fischer A, Pfeifer T. Extracting phase and amplitude modifications of laser-coupled Fano resonances. *Phys Rev Lett*. 2014;112(10):Article 103001.
9. He Y, Liu Z, Ott C, Pfeiffer AN, Sun S, Gaarde MB, Pfeifer T, Hu B. Resonant perfect absorption yielded by zero-area pulses. *Phys Rev Lett*. 2022;129(27):Article 273201.
10. Drescher L, Kornilov O, Witting T, Shokeen V, Vrakking MJJ, Schutte B. Extreme-ultraviolet spectral compression by four-wave mixing. *Nat Photonics*. 2021;15(4):263–266.
11. Li J, Liu Y. Hearing the heartbeat of atoms: Unveiling attosecond horizons. *Ultrafast Sci*. 2023;3:0049.
12. Wang L, Bai G, Wang X, Zhao J, Gao C, Wang J, Xiao F, Tao W, Song P, Qiu Q, et al. Raman time-delay in attosecond transient absorption of strong-field created krypton vacancy. *Nat Commun*. 2024;15(1):2705.
13. Reduzzi M, Chu WC, Feng C, Dubrouil A, Hummert J, Calegari F, Frassetto F, Poletto L, Kornilov O, Nisoli M, et al. Observation of autoionization dynamics and sub-cycle quantum beating in electronic molecular wave packets. *J Phys B Atomic Mol Phys*. 2016;49:Article 065102.
14. Sun M, Jiang Z, Fu Y, Jiang Y, Hu H, Bai C, Yue Z, Jiang J, Xie H, Jin C, et al. Observation of refractive index line shape in ultrafast XUV transient absorption spectroscopy. *Ultrafast Sci*. 2023;3:0029.
15. Liu Z, Cavaletto SM, Ott C, Meyer K, Mi Y, Harman Z, Keitel CH, Pfeifer T. Phase reconstruction of strong-field excited systems by transient-absorption spectroscopy. *Phys Rev Lett*. 2015;115(3):33003.
16. He Y, Liu Z, Cui Z, Zhang Y, Pfeiffer AN, Pfeifer T, Ding J, Hu B. Signatures of self-modulation effects during pulse propagation in single-pulse absorption spectra. *Phys Rev A*. 2019;99(5):Article 053418.
17. Han M, Liang H, Ji J, Sum CL, Ueda K, Rost JM, Wörner JH. Interference control of Fano resonances and dynamical imaging of an electron wave packet. *Ultrafast Sci*. 2025;5:Article 0091.
18. Peng P, Mi Y, Lytova M, Britton M, Ding X, Naumov AY, Corkum PB, Villeneuve DM. Coherent control of ultrafast extreme ultraviolet transient absorption. *Nat Photonics*. 2022;16(1):45–51.
19. Chini M, Zhao B, Wang H, Cheng Y, Hu SX, Chang Z. Subcycle AC stark shift of helium excited states probed with isolated attosecond pulses. *Phys Rev Lett*. 2012;109(7):Article 073601.
20. Chini M, Wang X, Cheng Y, Wu Y, Zhao D, Telnov DA, Chu S-I, Chang Z. Sub-cycle oscillations in virtual states brought to light. *Sci Rep*. 2013;3:1105.
21. Hütten K, Mittermair M, Stock SO, Beerwerth R, Shirvanyan V, Riemensberger J, Duensing A, Heider R, Wagner MS, et al. Ultrafast quantum control of ionization dynamics in krypton. *Nat Commun*. 2018;9(1):719.
22. Kraus PM, Mignolet B, Baykusheva D, Rupenyan A, Horný L, Penka EF, Grassi G, Tolstikhin OI, Schneider J, Jensen F, et al. Measurement and laser control of attosecond charge migration in ionized iodoacetylene. *Science*. 2015;350(6262):790–795.
23. Matselyukh DT, Despré V, Golubev NV, Kuleff AI, Wörner HJ. Decoherence and revival in attosecond charge migration driven by non-adiabatic dynamics. *Nat Phys*. 2022;18:1206–1213.
24. Pertot Y, Schmidt C, Matthews M, Chauvet A, Huppert M, Svoboda V, von Conta A, Tehlar A, Baykusheva D, Wolf J-P, et al. Time-resolved x-ray absorption spectroscopy with a water window high-harmonic source. *Science*. 2017;355(6322):264–267.
25. Kobayashi Y, Chang KF, Zeng T, Neumark DM, Leone SR. Direct mapping of curve-crossing dynamics in IBr by attosecond transient absorption spectroscopy. *Science*. 2019;365(6448):79–83.
26. Kobayashi Y, Neumark DM, Leone SR. Theoretical analysis of the role of complex transition dipole phase in XUV transient-absorption probing of charge migration. *Opt Express*. 2022;30(4):5673–5682.
27. Loh Z-H, Doumy G, Arnold C, Kjellsson L, Southworth SH, Al Haddad A, Kumagai Y, Tu M-F, Ho PJ, March AM, et al. Observation of the fastest chemical processes in the radiolysis of water. *Science*. 2020;367(6474):179–182.
28. Wu M, Chen S, Camp S, Schafer KJ, Gaarde MB. Theory of strong-field attosecond transient absorption. *J Phys B Atomic Mol Phys*. 2016;49(6):Article 062003.
29. Santra R, Yakovlev VS, Pfeifer T, Loh Z-H. Theory of attosecond transient absorption spectroscopy of strong-field-generated ions. *Phys Rev A*. 2011;83(3):Article 033405.
30. Pabst S, Sytcheva A, Moulet A, Wirth A, Goulielmakis E, Santra R. Theory of attosecond transient-absorption spectroscopy of krypton for overlapping pump and probe pulses. *Phys Rev A*. 2012;86(6):Article 063411.
31. Schultze M, Ramasesha K, Pemmaraju C, Sato SA, Whitmore D, Gandman A, Prell JS, Borja LJ, Prendergast D, Yabana K, et al. Attosecond band-gap dynamics in silicon. *Science*. 2014;346(6215):1348–1352.
32. Lucchini M, Sato SA, Ludwig A, Herrmann J, Volkov M, Kasmi L, Shinohara Y, Yabana K, Gallmann L, Keller U. Attosecond dynamical Franz-Keldysh effect in polycrystalline diamond. *Science*. 2016;353(6302):916–919.
33. Stapelfeldt H, Seideman T. Colloquium: Aligning molecules with strong laser pulses. *Rev Mod Phys*. 2003;75(2):543–557.

34. Safavi-Naeini AH, Mayer AP, Chan J, Eichenfield M, Winger M, Lin Q, Hill JT, Chang DE, Painter O. Electromagnetically induced transparency and slow light with optomechanics. *Nature*. 2011;472(7341):69–73.
35. Arimondo E. Coherent population trapping in laser spectroscopy. *Prog Opt*. 1996;35:257–354.
36. Yao J, Zeng B, Xu H, Li G, Chu W, Ni J, Zhang H, Chin SL, Cheng Y, Xu Z. High-brightness switchable multiwavelength remote laser in air. *Phys Rev A*. 2011;84(5):Article 051802.
37. Xu H, Lotstedt E, Iwasaki A, Yamanouchi K. Sub-10-fs population inversion in N_2^+ in air lasing through multiple state coupling. *Nat Commun*. 2015;6(1):Article 8347.
38. Britton M, Laferrière P, Ko DH, Li Z, Kong F, Brown G, Naumov A, Zhang C, Arissian L, Corkum P B. Testing the role of recollision in N_2^+ air lasing. *Phys Rev Lett*. 2018;120(13):Article 133208.
39. Zhang X, Lu Q, Zhang Z, Fan Z, Zhou D, Liang Q, Yuan L, Zhuang S, Dorfman K, Liu Y. Coherent control of the multiple wavelength lasing of N_2^+: Coherence transfer and beyond. *Optica*. 2021;8(5):668–673.
40. Arissian L, Kamer B, Rastegari A, Villeneuve DM, Diels JC. Transient gain from N_2^+ in light filaments. *Phys Rev A*. 2018;98(5):Article 053438.
41. Gao J, Liang H, Hasan M, Yuen CH, Tsai MS, Chen MC, Lin CD, Ueda K, Wörner HJ, Han M. Controlling rotational air lasing lineshape by carrier-envelope offset phase. *Nat Commun*. 2025;16(1):9654.
42. Richter F, Saalmann U, Allaria E, Wollenhaupt M, Ardini B, Brynes A, Callegari C, Cerullo G, Danailov M, Demidovich A. Strong-field quantum control in the extreme ultraviolet domain using pulse shaping. *Nature*. 2024;636(8042):337–341.

Ultrafast Science
A SCIENCE PARTNER JOURNAL

Line Shape Relations in Ultrafast Transient Absorption from a Coherent Superposition

Chunyuan Bai, Chun Huang, Hongtao Hu, Mathew Britton, Marianna Lytova, Zhongyao Yue, Xiaojing Liu, Ruxin Li, David M. Villeneuve, and Peng Peng

Citation: Bai C, Huang C, Hu H, Britton M, Lytova M, Yue Z, Liu X, Li R, Villeneuve D, Peng P. Line Shape Relations in Ultrafast Transient Absorption from a Coherent Superposition. *Ultrafast Sci*. 2026;**6**:0165. DOI: 10.34133/ultrafastscience.0165

Ultrafast laser pulses with broad bandwidth can simultaneously excite multiple quantum states, forming coherent superpositions. The phases of the associated optical transitions evolve in time, giving rise to spectral line profiles that range from symmetric Lorentzian to asymmetric Fano-like forms. Yet, the line shape relations between different transitions within such superpositions remain largely unexplored. Here, we use transient absorption spectroscopy to probe transitions from coherent superpositions. While each transition's line profile evolves over time, the relative line shape relations between different transitions remain fixed. We identify 4 fundamental types of line shape relations, each producing distinct spectral signatures. These relations naturally arise from second-order perturbation processes and can be actively tuned via the laser–matter interaction strength. Our findings establish a pathway for line shape-engineered control across atomic and molecular systems.
Image

Ultrafast Science (ISSN 2765-8791) is published by the American Association for the Advancement of Science. 1200 New York Avenue NW, Washington, DC 20005.

Supplementary Information

Line Shape Relations in Ultrafast Transient Absorption from a Coherent Superposition

Chunyuan Bai, Chun Huang, Hongtao Hu, Mathew Britton, Marianna Lytova, Zhongyao Yue, Xiaojing Liu, Ruxin Li, D. M. Villeneuve, Peng Peng*

* *e-mail address: pengpeng@shanghaitech.edu.cn*

Section 1: Separation of signals in the TAS of Rb

In the Rb experiment, since the pump and probe pulses share the same wavelength, it is essential to carefully block the pump beam during the spectral measurement to ensure that it does not contaminate the probe signal. Therefore, we employ a non-collinear geometry, as shown in Fig. R1. A 3 mrad non-collinear crossing angle was chosen to ensure sufficient spatial overlap of the two beams throughout the 50-mm Rb cell, while allowing clear spatial separation at the collection optics located 2 m downstream. The required light intensity in this experiment is relatively low ($\sim 10^9$ W/cm^2), and both the pump and probe beams are kept collimated with a beam diameter of 2 mm. The two pulses fully overlap at the center of the Rb cell. The maximum spatial walk-off within the 50 mm cell is estimated to be $\Delta X = 25\ \text{mm} \times \tan(3\ \text{mrad}) \approx 75\ \mu\text{m}$, which is much smaller than the beam diameter. Therefore, the effective overlap length can be approximated $L = 50\ mm$ (the full length of the Rb cell). At the detection plane, the beam separation is $\Delta S = 2000\ \text{mm} \times \tan(3\ \text{mrad}) \approx 6\ \text{mm}$, which is significantly larger than the beam diameter, indicating that the two beams are fully separated in space. A baffle is used to block the direct pump beam, allowing only the probe beam to enter the integrating sphere. In addition, an aperture is placed in front of the integrating sphere to further suppress scattered light.

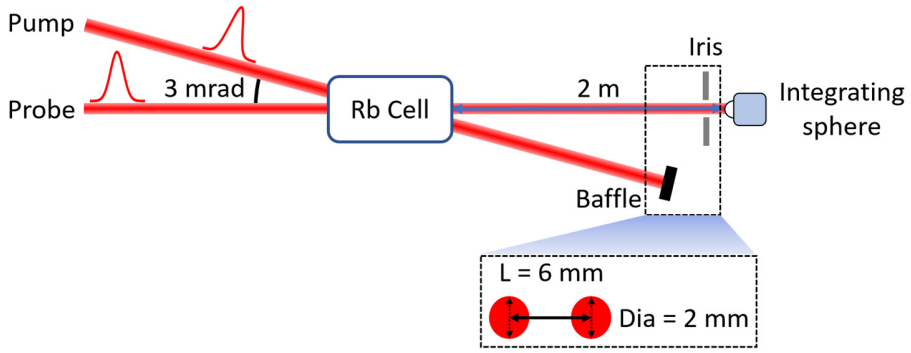

Fig. S1. Schematic of the Rb experimental setup. The baffle, iris, and integrating sphere are positioned 2 m downstream from the Rb cell to ensure effective separation of the two beams. The pump beam is carefully blocked during spectral measurements to prevent contamination of the probe signal.

Section 2: Fourier filtering

In our pump-probe experiment, the pump pulse induces both population transfer among states and quantum coherences between them. The population dynamics are typically slow and largely independent of the pump-probe delay, reflecting quasi-steady-state redistribution of population. In contrast, the coherence dynamics are fast and strongly delay-dependent, arising from the quantum beat between different states [1,2]. The experimental observable, the differential optical density, is defined as: $\Delta\text{OD}(\omega,\tau) = -\log[I_{on}(\omega,\tau)/I_{off}(\omega,\tau)]$, where ω is the photon energy, τ is the pump-probe delay, $I_{on}(\omega,\tau)$ and $I_{off}(\omega,\tau)$ are the transmitted probe spectra with and without the pump, respectively. This signal inherently contains contributions from both population changes and quantum coherences. By applying a Fourier filter to ΔOD, we can isolate the delay-dependent

component. This enables a more precise analysis of line shape changes induced by quantum coherences.

Fig. S2(a) shows the original ΔOD signal for Rb. Fig. S2(b) displays the corresponding two-dimensional Fourier transform spectrum. The spectral features near 0 THz arise from the delay-independent population changes, while the peaks around 7 THz correspond to delay-dependent quantum coherences between $5p_{1/2}$ and $5p_{3/2}$ states [3]. To isolate the coherence signal, a bandpass filter from 5 THz to 9 THz was applied. The resulting filtered signal, shown in Fig. S2(c) (same as Fig. 2b in the main text), clearly highlights the quantum beat dynamics.

Similarly, Fig. S3(a) and Fig. S3(b) show the original ΔOD signal and its Fourier transform spectrum for H_2. The dominant beating frequency at 17 THz corresponds to quantum coherences between $X^1\Sigma_g^+(v=0, J=1)$ and $X^1\Sigma_g^+(v=0, J=3)$ states. A bandpass filter from 14 THz to 20 THz was applied to emphasize the quantum beat signal. Fig. S3(c) shows the filtered signal (same as Fig. 3b in the main text).

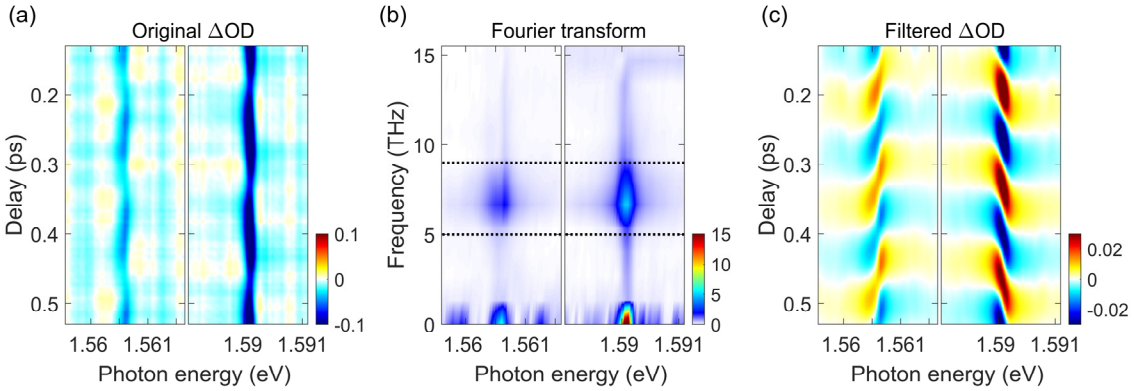

Fig. S2. Fourier filtering of Rb quantum beat signal. (a) Original ΔOD signal. **(b)** Two-dimensional Fourier transform spectrum. The applied bandpass filter (5-9 THz) is indicated by dotted black lines. **(c)** Filtered ΔOD signal, highlighting the quantum beat oscillations between $5p_{1/2}$ and $5p_{3/2}$ states (same as Fig. 2b in the main text).

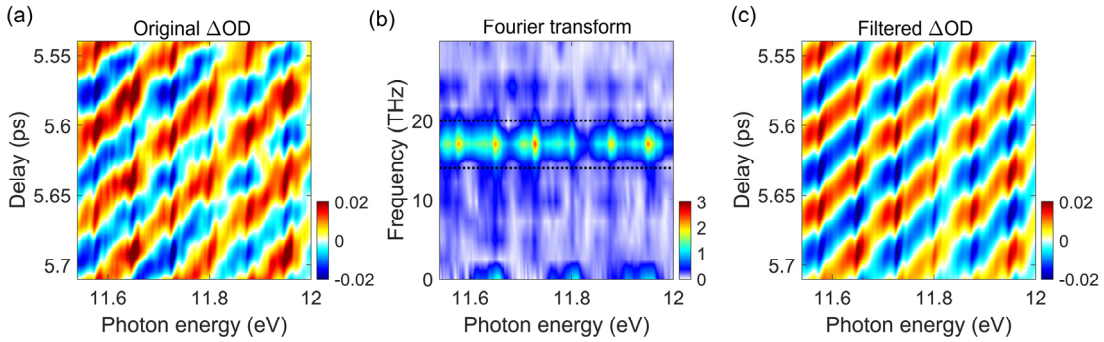

Fig. S3. Fourier filtering of H_2 quantum beat signal. (a) Original ΔOD signal. **(b)** Two-dimensional Fourier transform spectrum. The applied bandpass filter (14-20 THz) is indicated by dotted black lines. **(c)** Filtered ΔOD signal, highlighting the quantum beat oscillations between $X^1\Sigma_g^+(v=0, J=1)$ and $X^1\Sigma_g^+(v=0, J=3)$ states (same as Fig. 3b in the main text).

Section 3: Fitted ΔOD through line-shape analysis

As described in the Method section of the main text, the measured absorption line shape is fitted with $\sigma(\omega,\tau) = a\left\{\cos[\phi(\tau)]\frac{\frac{\Gamma}{2}}{(\omega_0-\omega)^2+\frac{\Gamma^2}{4}} + \sin[\phi(\tau)]\frac{(\omega_0-\omega)}{(\omega_0-\omega)^2+\frac{\Gamma^2}{4}}\right\} + b$. Representative one-dimensional slices of the measured and fitted spectra are shown in Fig. 2d and Fig. 3d of the main text. Here, we present the full two-dimensional comparison in Fig. S4, illustrating the excellent agreement between the experimental and fitted line shapes across all pump-probe delays.

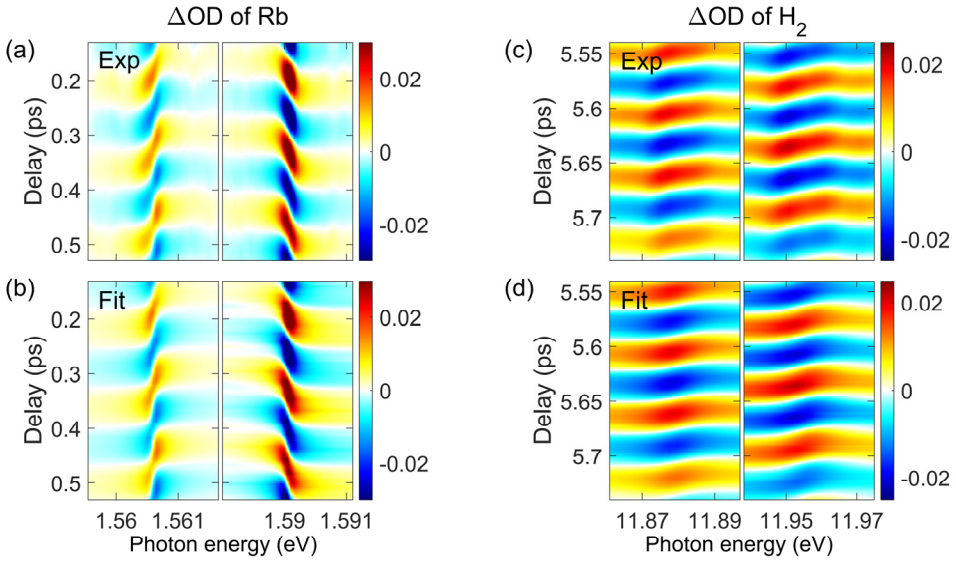

Fig. S4. Experimental and fitted differential absorption of Rb and H_2. (a) Experimental ΔOD of Rb. **(b)** Fitted ΔOD of Rb. **(c)** Experimental ΔOD of H_2. **(d)** Fitted ΔOD of H_2.

Section 4: Analysis model based on the second order perturbation theory

Consider a generic three-level system with states labeled 'a', 'b' and 'c', with corresponding eigenenergies E_a, E_b and E_c, respectively. A pump pulse creates a superposition between 'b' and 'c', a subsequent probe pulse couples this superposition to state 'a' at delay τ, as shown in Fig. S5. The wavefunction of the electron in this system is expressed as:

$$|\psi(t,\tau)\rangle = C_a(t,\tau)|\psi_a\rangle + C_b(t,\tau)|\psi_b\rangle + C_c(t,\tau)|\psi_c\rangle, \quad \text{(S1)}$$

where C_a, C_b and C_c are the complex probability amplitudes, and $|\psi_a\rangle$, $|\psi_b\rangle$ and $|\psi_c\rangle$ are the eigenfunctions of the three levels, respectively.

In the case of H_2, prior to the arrival of the probe XUV pulse, state 'a' is unpopulated. In contrast, for Rb, all three levels retain nonzero populations after pump excitation. Accordingly, the models for H_2 and Rb are treated separately.

4.1 Model for H_2

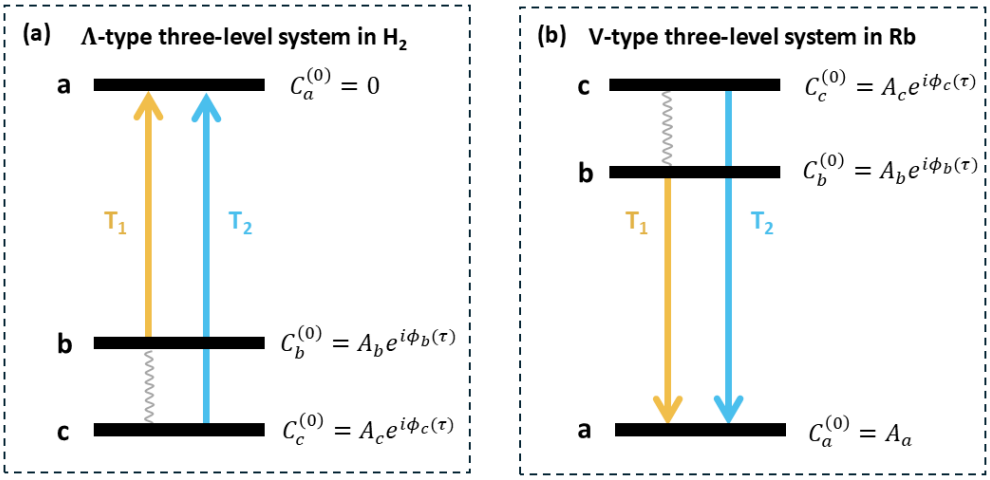

Fig. S5. Schematic diagrams of the Λ-type (a) & V-type (b) three-level systems. $C_a^{(0)}$, $C_b^{(0)}$ and $C_c^{(0)}$ are the complex probability amplitudes before the arrival of the probe pulse.

For H_2, the superposition between 'b' and 'c' evolves freely before the probe pulse. The complex probability amplitudes are given by:

$$C_a^{(0)} = 0, C_b^{(0)} = A_b e^{i\phi_b(\tau)}, C_c^{(0)} = A_c e^{i\phi_c(\tau)}, \tag{S2}$$

where A_b and A_c are the amplitudes, and $\phi_b(\tau) = -E_b\tau$ and $\phi_c(\tau) = -E_c\tau$ are the phases of the respective states (atomic units are used throughout, unless otherwise noted).

When the probe pulse arrives, all three levels are coupled, and the corresponding Hamiltonian is

$$\hat{H}(t) = \begin{bmatrix} E_a & -\mu_{ab}E(t) & -\mu_{ac}E(t) \\ -\mu_{ba}E(t) & E_b & 0 \\ -\mu_{ca}E(t) & 0 & E_c \end{bmatrix}, \tag{S3}$$

where μ_{ab} and μ_{ac} are the transition matrix elements, $E(t)$ is the probe field. Given that the probe-matter interaction is impulsive and weak, $E(t)$ is approximated as a delta function. The probability amplitudes $C_i(t)$ $(i = a, b, c)$ can be expressed as $C_i(t) = C_i^{(0)}(t) + C_i^{(1)}(t) + C_i^{(2)}(t)$, where $C_i^{(n)}(t)$ denotes the nth-order contribution in the perturbative expansion. These terms can be calculated using the recursion formula of second-order time-dependent perturbation theory [4],

$$\begin{aligned} C_i^{(0)}(t) &= C_i^{(0)} \\ C_i^{(1)}(t) &= -\frac{i}{\hbar}\sum_{m\neq i}\int_{-\infty}^{t} dt' \langle i|H(t')|m\rangle e^{i\omega_{im}t'} C_m^{(0)}(t'), \\ C_i^{(2)}(t) &= -\frac{i}{\hbar}\sum_{m\neq i}\int_{-\infty}^{t} dt' \langle i|H(t')|m\rangle e^{i\omega_{im}t'} C_m^{(1)}(t'). \end{aligned} \tag{S4}$$

Under the delta-function approximation for the probe field, the probability amplitudes are:

$$
\begin{aligned}
C_a(t,\tau) &= i\left[A_c\Omega_{ca}e^{i\phi_c(\tau)} + A_b\Omega_{ba}e^{i\phi_b(\tau)}\right]e^{-iE_at} \\
C_b(t,\tau) &= \left[A_be^{i\phi_b(\tau)} - \Omega_{ba}\left(A_b\Omega_{ba}e^{i\phi_b(\tau)} + A_c\Omega_{ca}e^{i\phi_c(\tau)}\right)\right]e^{-iE_bt}, \\
C_c(t,\tau) &= \left[A_ce^{i\phi_c(\tau)} - \Omega_{ca}\left(A_b\Omega_{ba}e^{i\phi_b(\tau)} + A_c\Omega_{ba}e^{i\phi_c(\tau)}\right)\right]e^{-iE_ct},
\end{aligned}
\tag{S5}
$$

where $\Omega = \mu\int_{-\infty}^{\infty} f(t)\,dt$, μ is the value of transition dipole and $f(t)$ is the envelope of probe pulse. The free induction decay (FID) is given by $d(t) = \langle\psi(t,\tau)|r|\psi(t,\tau)\rangle$, for transitions T_1 ($'b' \to 'a'$) and T_2 ($'c' \to 'a'$), they are expressed as

$$
d_{ba}(t,\tau) = 2Re\left\{i\mu_{ba}\begin{pmatrix} A_b^2\Omega_{ba}(1-|\Omega_{ba}|^2) \\ +A_c^2\Omega_{ba}|\Omega_{ca}|^2e^{i\pi} \\ +A_cA_b\Omega_{ca}(1-|\Omega_{ba}|^2)e^{i[\phi_c(\tau)-\phi_b(\tau)]} \\ +A_cA_b\Omega_{ca}|\Omega_{ba}|^2e^{i[\phi_b(\tau)-\phi_c(\tau)+\pi]} \end{pmatrix}e^{i(E_b-E_a)t-\Gamma_{ba}t}\right\}, \tag{S6a}
$$

$$
d_{ca}(t,\tau) = 2Re\left\{i\mu_{ca}\begin{pmatrix} A_c^2\Omega_{ca}(1-|\Omega_{ca}|^2) \\ +A_b^2\Omega_{ca}|\Omega_{ba}|^2e^{i\pi} \\ +A_cA_b\Omega_{ba}(1-|\Omega_{ca}|^2)e^{i[\phi_b(\tau)-\phi_c(\tau)]} \\ +A_cA_b\Omega_{ba}|\Omega_{ca}|^2e^{i[\phi_c(\tau)-\phi_b(\tau)-\pi]} \end{pmatrix}e^{i(E_c-E_a)t-\Gamma_{ca}t}\right\}, \tag{S6b}
$$

where Γ is the decoherence rate. The corresponding absorption cross section is calculated by $\sigma(\omega) \propto Im[d(\omega)]$, where $d(\omega)$ is the Fourier transform of $d(t)$,

$$
\sigma_{ba}(\omega,\tau) \propto Im\left\{\begin{pmatrix} A_b^2\Omega_{ba}(1-|\Omega_{ba}|^2) \\ +A_c^2\Omega_{ba}|\Omega_{ca}|^2e^{i\pi} \\ +A_cA_b\Omega_{ca}(1-|\Omega_{ba}|^2)e^{i[\phi_c(\tau)-\phi_b(\tau)]} \\ +A_cA_b\Omega_{ca}|\Omega_{ba}|^2e^{i[\phi_b(\tau)-\phi_c(\tau)+\pi]} \end{pmatrix}\frac{1}{(E_a-E_b-\omega)-i\frac{\Gamma_{ba}}{2}}\right\}, \tag{S7a}
$$

$$
\sigma_{ca}(\omega,\tau) \propto Im\left\{\begin{pmatrix} A_c^2\Omega_{ca}(1-|\Omega_{ca}|^2) \\ +A_b^2\Omega_{ca}|\Omega_{ba}|^2e^{i\pi} \\ +A_cA_b\Omega_{ba}(1-|\Omega_{ca}|^2)e^{i[\phi_b(\tau)-\phi_c(\tau)]} \\ +A_cA_b\Omega_{ba}|\Omega_{ca}|^2e^{i[\phi_c(\tau)-\phi_b(\tau)-\pi]} \end{pmatrix}\frac{1}{(E_a-E_c-\omega)-i\frac{\Gamma_{ca}}{2}}\right\}. \tag{S7b}
$$

Each FID signal in Eq. S6 and the corresponding absorption cross section in Eq. S7 comprises four terms: among which only the last two are delay-dependent anfend related to the measured ΔOD signals. We define the delay-dependent FID signal as $d_{Dyn}(t,\tau)$, given by

$$
d_{Dyn,ba}(t,\tau) = 2Re\left\{i\mu_{ba}A_cA_b\Omega_{ca}\begin{pmatrix}(1-|\Omega_{ba}|^2)e^{i[\phi_c(\tau)-\phi_b(\tau)]} \\ +|\Omega_{ba}|^2e^{i[\phi_b(\tau)-\phi_c(\tau)+\pi]}\end{pmatrix}e^{i(E_b-E_a)t-\Gamma_{\mathrm{ba}}t}\right\}, \tag{S8a}
$$

$$
d_{Dyn,ca}(t,\tau) = 2Re\left\{i\mu_{ca}A_cA_b\Omega_{ba}\begin{pmatrix}(1-|\Omega_{ca}|^2)e^{i[\phi_b(\tau)-\phi_c(\tau)]} \\ +|\Omega_{ca}|^2e^{i[\phi_c(\tau)-\phi_b(\tau)-\pi]}\end{pmatrix}e^{i(E_c-E_a)t-\Gamma_{\mathrm{ca}}t}\right\}. \tag{S8b}
$$

These expressions are identical to Eq. 1 and Eq. 2 in the main text. Each $d_{Dym}(t,\tau)$ comprises two phase-dependent terms, as summarized in Table S1. The combination between these terms gives rise to four distinct phase relations.

Table S1: Summary of four kinds of phase relations.

$d_{Dyn,ca}$ \ $d_{Dyn,ba}$	$\phi_c(\tau)-\phi_b(\tau)$	$\phi_b(\tau)-\phi_c(\tau)+\pi$
$\phi_b(\tau)-\phi_c(\tau)$	*c.c.* relation	anti-π relation
$\phi_c(\tau)-\phi_b(\tau)-\pi$	π relation	anti-*c.c.* relation

4.2 Model for Rb

For Rb, the complex probability amplitudes prior to probe pulse are:

$$C_a^{(0)} = A_a, C_b^{(0)} = A_b e^{i\phi_b(\tau)}, C_c^{(0)} = A_c e^{i\phi_c(\tau)}. \tag{S9}$$

When the probe pulse arrives, the corresponding Hamiltonian is:

$$\widehat{H}(t) = \begin{bmatrix} E_c & 0 & -\mu_{ac}E(t) \\ 0 & E_b & -\mu_{ab}E(t) \\ -\mu_{ca}E(t) & -\mu_{ab}E(t) & E_a \end{bmatrix}. \tag{S10}$$

Using the recursion formula in Eq. S4, the probability amplitudes are given by:

$$\begin{aligned} C_a(t,\tau) &= \left\{A_a(1-\Omega_{ba}^2-\Omega_{ca}^2) + i\left[A_b\Omega_{ba}e^{i\phi_b(\tau)} + A_c\Omega_{ca}e^{i\phi_c(\tau)}\right]\right\}e^{-iE_a t}, \\ C_b(t,\tau) &= \left[A_b e^{i\phi_b(\tau)} + iA_a\Omega_{ba} - \Omega_{ba}\left(A_b\Omega_{ba}e^{i\phi_b(\tau)} + A_c\Omega_{ca}e^{i\phi_c(\tau)}\right)\right]e^{-iE_b t}, \\ C_c(t,\tau) &= \left[A_c e^{i\phi_c(\tau)} + iA_a\Omega_{ca} - \Omega_{ca}\left(A_b\Omega_{ba}e^{i\phi_b(\tau)} + A_c\Omega_{ba}e^{i\phi_c(\tau)}\right)\right]e^{-iE_c t}. \end{aligned} \tag{S11}$$

The free induction decay for transitions $T_1('b' \to 'a')$ and $T_2('c' \to 'a')$ are expressed as:

$$d_{ba}(t,\tau) = 2Re\left\{ i\mu_{ba} \begin{pmatrix} A_b^2\Omega_{ba}(1-|\Omega_{ba}|^2) \\ +A_c^2\Omega_{ba}|\Omega_{ca}|^2 e^{i\pi} \\ +A_a^2\Omega_{ba}Ze^{i\pi} \\ +A_aA_b|\Omega_{ba}|^2 e^{i\left[\phi_b(\tau)-\frac{\pi}{2}\right]} \\ +A_aA_c\Omega_{ba}\Omega_{ca}e^{i\left[\phi_c(\tau)-\frac{\pi}{2}\right]} \\ +A_aA_b(1-|\Omega_{ba}|^2)Ze^{-i\left[\phi_b(\tau)+\frac{\pi}{2}\right]} \\ +A_aA_c\Omega_{ba}\Omega_{ca}Ze^{i\left[\phi_c(\tau)+\frac{\pi}{2}\right]} \\ +A_cA_b\Omega_{ca}(1-|\Omega_{ba}|^2)e^{i[\phi_c(\tau)-\phi_b(\tau)]} \\ +A_cA_b\Omega_{ca}|\Omega_{ba}|^2 e^{i[\phi_b(\tau)-\phi_c(\tau)+\pi]} \end{pmatrix} e^{i(E_b-E_a)t-\Gamma_{ba}t} \right\} \tag{S12a}$$

$$d_{ca}(t,\tau) = 2Re\left\{ i\mu_{ca} \begin{pmatrix} A_c^2\Omega_{ca}(1-|\Omega_{ca}|^2) \\ +A_b^2\Omega_{ca}|\Omega_{ba}|^2 e^{i\pi} \\ +A_a^2\Omega_{ca} Z e^{i\pi} \\ +A_a A_b \Omega_{ba}\Omega_{ca} e^{i\left[\phi_b(\tau)-\frac{\pi}{2}\right]} \\ +A_a A_c |\Omega_{ca}|^2 e^{i\left[\phi_c(\tau)-\frac{\pi}{2}\right]} \\ +A_a A_b \Omega_{ba}\Omega_{ca} Z e^{i\left[\phi_b(\tau)+\frac{\pi}{2}\right]} \\ +A_a A_c Z(1-|\Omega_{ca}|^2) e^{-i\left[\phi_c(\tau)+\frac{\pi}{2}\right]} \\ +A_c A_b \Omega_{ba}(1-|\Omega_{ca}|^2) e^{i[\phi_b(\tau)-\phi_c(\tau)]} \\ +A_c A_b \Omega_{ba}|\Omega_{ca}|^2 e^{i[\phi_c(\tau)-\phi_b(\tau)+\pi]} \end{pmatrix} e^{i(E_c-E_a)t-\Gamma_{ca}t} \right\}, \quad \text{(S12b)}$$

where $Z = 1 - |\Omega_{ba}|^2 - |\Omega_{ca}|^2$. FID signals in Eq. S12a and Eq. S12b consist of nine terms. The first three are delay independent. Terms 4–7 oscillate rapidly with a period of ~ 2.7 fs, much shorter than the experimental temporal resolution (~ 10 fs), and therefore average to zero. Consequently, the experimentally measured ΔODin Rb arises only from the last two terms, as in the Λ-type three-level system of H_2. Each transition contains two phase-dependent contributions: $T_1, \phi_c(\tau) - \phi_b(\tau)$ and $\phi_b(\tau) - \phi_c(\tau) + \pi$; $T_2, \phi_b(\tau) - \phi_c(\tau)$ and $\phi_c(\tau) - \phi_b(\tau) + \pi$. The combinations of these contributions give rise to four distinct phase relations, as summarized in Table S1.

Section 5: Mixed phase relations

In Fig. 4 of the main text, the sum $\phi_1(\tau) + \phi_2(\tau)$ and difference $\phi_1(\tau) - \phi_2(\tau)$ of the extracted line-shape phases exhibit weak oscillations around 0 and π, respectively. This behavior arises from a mixed phase effect, in which the parameter $|\Omega|^2$ in Eq. S8a and Eq. S8b is neither 0 nor 1. In this intermediate regime, two phase-dependent terms contribute simultaneously to the measured transient absorption signals. The delay-dependent absorption cross section is given by $\sigma_{Dyn}(\omega,\tau) \propto Im[d_{Dyn}(\omega,\tau)]$, where $d_{Dyn}(\omega,\tau)$ is the Fourier transform of $d_{Dyn}(t,\tau)$. Specifically:

$$\sigma_{Dyn,ba}(\omega,\tau) \propto Im\left\{ \begin{pmatrix} (1-|\Omega_{ba}|^2) e^{i[\phi_c(\tau)-\phi_b(\tau)]} \\ +|\Omega_{ba}|^2 e^{i[\phi_b(\tau)-\phi_c(\tau)+\pi]} \end{pmatrix} \frac{1}{(E_a - E_b - \omega) - i\frac{\Gamma_{ba}}{2}} \right\}, \quad \text{(S13a)}$$

$$\sigma_{Dyn,ca}(\omega,\tau) \propto Im\left\{ \begin{pmatrix} (1-|\Omega_{ca}|^2) e^{i[\phi_b(\tau)-\phi_c(\tau)]} \\ +|\Omega_{ca}|^2 e^{i[\phi_c(\tau)-\phi_b(\tau)+\pi]} \end{pmatrix} \frac{1}{(E_a - E_c - \omega) - i\frac{\Gamma_{ca}}{2}} \right\}. \quad \text{(S13b)}$$

By fitting the experimental spectra with Eq. S13, we extract the values of $|\Omega|^2$. Using the parameters: $E_a = 0$ eV, $E_b = 1.56$ eV, $E_c = 1.59$ eV, $\Gamma_{\mathrm{ba}} = \Gamma_{ca} = 0.15$ meV, $\phi_b(\tau) = -E_b\tau$ and $\phi_c(\tau) = -E_c\tau$, we find $|\Omega_{ba}|^2 = 0.2$, $|\Omega_{ca}|^2$ =0. The resulting $\sigma_{Dyn,ba}(\omega,\tau)$ and $\sigma_{Dyn,ca}(\omega,\tau)$ calculated from these values are shown in Fig. S6(a). Using Eq. 1 in the main text, we extract the line-shape phases $\phi_1(\tau)$ and $\phi_2(\tau)$, represented by red and blue dots in Fig. S6(b).

The observed oscillation of $\phi_1(\tau) + \phi_2(\tau)$ around zero agrees well with the experimental results presented in Fig. 4a of the main text.

This effect is also observed in the phase relation control experiments. Similarly, we extracted the values of $|\Omega|^2$ by fitting the experimental spectra with Eq. S13. Fig. S7(a)-(d) show the experimental results, with the corresponding $|\Omega|^2$ values indicated at the bottom of each spectrum. Using these extracted values, we calculated $\sigma_{Dyn,ba}(\omega,\tau)$ and $\sigma_{Dyn,ca}(\omega,\tau)$, which are shown in Fig. S7(e)-(f).

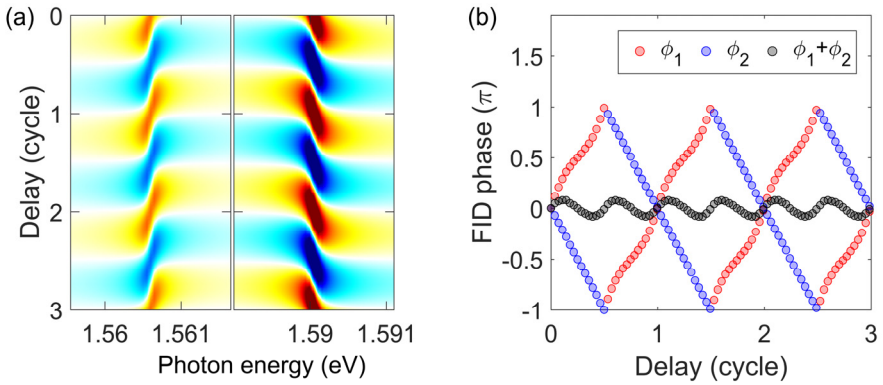

Fig. S6. Mixed phase relation. (a) Calculated delay-dependent absorption cross section $\sigma_{Dyn,ba}(\omega,\tau)$ and $\sigma_{Dyn,ca}(\omega,\tau)$ by using $|\Omega_{ba}|^2 = 0.2$, $|\Omega_{ca}|^2$=0. **(b)** Extracted line-shape phase by using Eq. 1 in the main text. The sum $\phi_1(\tau) + \phi_2(\tau)$ oscillate around zero, well agrees with experimental results shown in Fig. 4 of the main text.

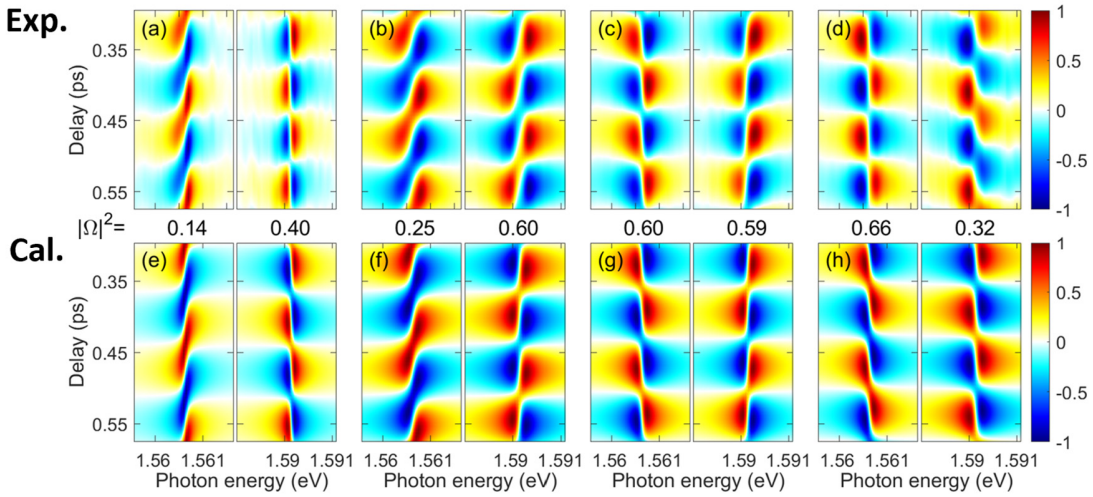

Fig. S7. Phase relation control in Rb. (a)-(d) Experimental transient absorption spectra. Four distinct structures were observed, the hat, twill, inverted-hat and inverted-twill features, respectively. The extracted value of $|\Omega|^2$ is shown on the bottom of each spectrum. **(e)-(f)** Calculated delay-dependent absorption cross section.

Section 6: Numerical simulation based on density matrix

The evolution of the three-level system described in Section 4 was simulated by numerically solving the Liouville-von Neumann equation:

$$\frac{d\hat{\rho}(t)}{dt} = -\frac{i}{\hbar}\left[\hat{H}(t), \hat{\rho}(t)\right]. \tag{S14}$$

The Hamiltonian $\hat{H}(t)$ is given by: $\hat{H}(t) = \begin{bmatrix} E_a & -\mu_{ab}E(t) & -\mu_{ac}E(t) \\ -\mu_{ba}E(t) & E_b & 0 \\ -\mu_{ca}E(t) & 0 & E_c \end{bmatrix}$, where μ_{ab} and μ_{ac} are the transition matrix elements, and $E(t)$ is the probe field. The energy levels are set to $E_a = 0$ eV, $E_b = -11.45$ eV and $E_c = -11.95$ eV. The initial probe electric field $E_0(t)$ is a transform-limited Gaussian pulse with the duration $\tau = 1$ fs, the peak intensity $I_0 = 2 \times 10^{10}$ W/cm^2, and the central photon energy $\omega_0 = 12.4$ eV.

The density matrix is represented as: $\hat{\rho}(t) = \begin{bmatrix} \rho_{aa} & \rho_{ab} & \rho_{ac} \\ \rho_{ba} & \rho_{bb} & \rho_{bc} \\ \rho_{ca} & \rho_{cb} & \rho_{cc} \end{bmatrix}$, where the diagonal elements are the populations, and the off-diagonal elements are the coherences between states. The initial density matrix is assumed as $\rho_{aa}(0) = 0$, $\rho_{bb}(0) = 0.5$ and $\rho_{cc}(0) = 0.5$, with all coherences initially zero in the absence of a pump pulse. When a preceding pump pulse is included, it establishes an initial coherence $\rho_{bc}(0) = 0.25e^{-i(E_b - E_c)\tau}$ between the 'b' and 'c' states, where τ is the pump-probe delay.

The equations of motion are solved numerically using the Crank–Nicolson method. The medium polarization is computed as $P = N \times Tr(\hat{\rho}\hat{\mu})$, where N is the number density. The polarization acts as a source term in the one-dimensional wave equation for the probe field, expressed in the probe's reference frame as:

$$\frac{\partial E(t,z)}{\partial z} = -\left(\frac{1}{c} - \frac{1}{v_g}\right)\frac{\partial E(t,z)}{\partial t} - \frac{2\pi}{c}\frac{\partial P(t,z)}{\partial t}. \tag{S15}$$

Here, c is the speed of light, v_g is the group velocity. A single propagation step of 0.08 μm in a density of 10^{18} cm^{-3} is sufficient to generate a free induction decay signal. Propagation includes first- and second-order changes to the electric field and is suitable for many propagation steps, but the calculation uses a single step to accommodate the computation time. The transmitted probe spectrum is calculated as $I(\omega) = |E(\omega)|^2$, then convolved with the experimental resolution function: $I_c(\omega) = I(\omega) \otimes G(\omega)$, where $G(\omega) = e^{-4\ln 2\left(\frac{\omega}{\delta\omega}\right)^2}$ and $\delta\omega = 15$ meV.

Simulations are performed both with $[I_{c,on}(\omega)]$ and without $[I_{c,off}(\omega)]$ the pump excitation. The predicted differential absorption spectrum is calculated in the same way as for the experimental data: $\Delta\text{OD} = -\log\left[\frac{I_{c,on}(\omega)}{I_{c,off}(\omega)}\right]$.

By varying the magnitude of $|\Omega|^2$, the simulation results for the four phase relations are obtained, as shown in Fig. S8. Four distinct structures were observed, the hat, twill, inverted-hat and inverted-twill, corresponding to the *c.c.*, π, anti-*c.c.*, and anti-π phase relations, respectively.

These simulation results are in excellent agreement with the theoretical predictions and experimental observations presented in Fig. 5 of the main text.

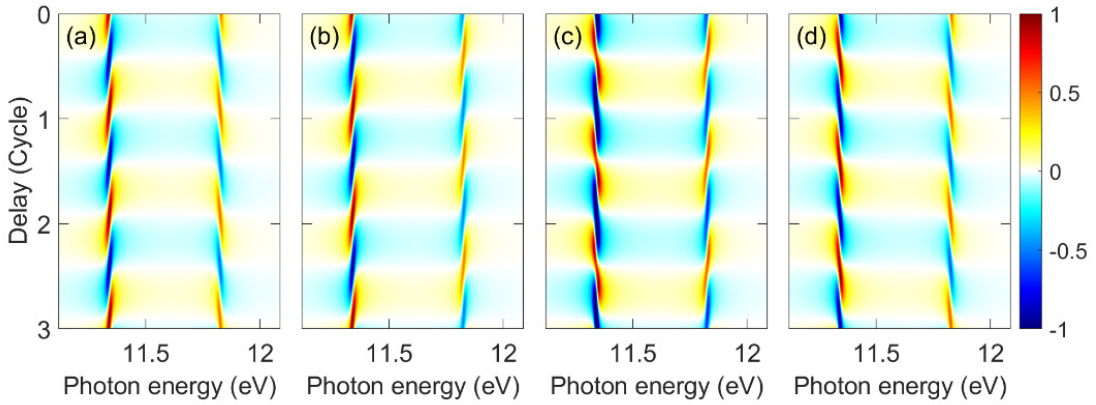

Fig. S8. Calculated differential absorption spectra ΔOD. **(a)** $|\Omega_{ba}|^2 = 0.02$, $|\Omega_{ca}|^2 = 0.02$. **(b)** $|\Omega_{ba}|^2 = 0.02$, $|\Omega_{ca}|^2 = 0.84$. **(c)** $|\Omega_{ba}|^2 = 0.84$, $|\Omega_{ca}|^2 = 0.02$. **(d)** $|\Omega_{ba}|^2 = 0.84$, $|\Omega_{ca}|^2 = 0.84$. The calculations use atomic units.

References

1. Santra R, Yakovlev VS, Pfeifer T, Loh Z-H. Theory of attosecond transient absorption spectroscopy of strong-field-generated ions. *Phys Rev A.* 2011;83(3):Article 033405.

2. Goulielmakis E, Loh Z-H, Wirth A, Santra R, Rohringer N, Yakovlev VS, Zherebtsov S, Pfeifer T, Azzeer AM, Kling MF, et al. Real-time observation of valence electron motion. *Nature*. 2010;466(7307):739-743.

3. Liu Z, Cavaletto S M, Ott C, Meyer K, Mi Y, Harman Z, Keitel C H, Pfeifer T. Phase reconstruction of strong-field excited systems by transient-absorption spectroscopy. *Phys Rev Lett.* 2015;115(3):Article 33003

4. Sakurai JJ. Modern Quantum Mechanics. MA: Addison-Wesley Pub., 1994. ISBN: 9780201539295.